IEEE Access
Multidisciplinary | Rapid Review | Open Access Journal

Received 2 January 2023, accepted 9 January 2023, date of publication 13 January 2023, date of current version 20 January 2023.

Digital Object Identifier 10.1109/ACCESS.2023.3236821

APPLIED RESEARCH

OpenRST: An Open Platform for Customizable 3D Printed Cable-Driven Robotic Surgical Tools

JACINTO COLAN[1], (Member, IEEE), ANA DAVILA[2], (Member, IEEE), YAONAN ZHU[1], (Member, IEEE), TADAYOSHI AOYAMA[1], (Member, IEEE), AND YASUHISA HASEGAWA[1], (Member, IEEE)

[1]Department of Micro-Nano Mechanical Science and Engineering, Nagoya University, Furo-cho, Chikusa-ku, Nagoya 464-8603, Japan
[2]Institutes of Innovation for Future Society, Nagoya University, Furo-cho, Chikusa-ku, Nagoya 464-8601, Japan

Corresponding author: Jacinto Colan (colan@robo.mein.nagoya-u.ac.jp)

This work was supported in part by the Japan Science and Technology Agency (JST) CREST including AIP Challenge Program under Grant JPMJCR20D5, and in part by the Japan Society for the Promotion of Science (JSPS) Grants-in-Aid for Scientific Research (KAKENHI) under Grant 22K14221.

ABSTRACT Robot-assisted minimally invasive surgery (RMIS) has been shown to be effective in improving surgeon capabilities, providing magnified 3D vision, highly dexterous surgical tools, and intuitive human-robot interfaces for high-precision tool motion control. Robotic surgical tools (RST) are a critical component that defines the performance of an RMIS system. Current RSTs still represent a high cost, with few commercially available options, which limits general access and research on RMIS. We aim to take advantage of recent progress in biocompatible 3D printing and contribute to the development of RMIS technologies, presenting an open platform for low-cost, biocompatible, and customizable RSTs. The proposed design concept consists of a 3-DOF end-effector with a decoupled wrist mechanism, a tool interface module, and a tool drive unit. We validated our end-effector design using Finite Element Analysis (FEA) to confirm that stress generated by high grip forces is maintained below the material yield stress. Validation experiments showed that the proposed RST could provide up to 10N grip forces and up to 3N pulling forces. The proposed control framework exhibited a mean absolute positioning tracking error of approximately 0.1 rad. Finally, we also demonstrated the use of the proposed RST in two surgical training tasks: pick-and-place and stitching. The designs and software control framework are open-access and freely available for customization and fast development at https://github.com/jcolan/OpenRST.

INDEX TERMS 3D printing, cable-driven tool, minimally invasive surgery, robot-assisted surgery, surgical instrument.

I. INTRODUCTION

Minimally invasive surgery (MIS) is a standard surgical procedure in which surgical tools are inserted into the body of the patient through small incisions or ports. MIS offers many advantages over traditional open surgery: it reduces trauma and scarring and shortens recovery time. However, MIS is subject to several drawbacks, including loss of depth perception, poor eye-hand coordination, limited range of motion, and lack of tool dexterity [1]. Robotic-assisted minimally invasive surgical systems (RMIS) have been shown to be effective in addressing these problems, providing magnified 3D vision with depth perception, highly dexterous surgical tools, and intuitive human-robot interfaces with improved ergonomics and high-precision tool motion control [2]. Surgical robotic systems used in RMIS usually follow a multiport procedure setup, in which multiple robotic manipulators hold a robotic surgical tool (RST) that is introduced into the body through small ports. The surgeon then controls the position and orientation of the RST end-effector and the opening angle of the grasper through an interface mounted directly on the surgical tool [3] or remotely from a teleoperation console [4].

The performance achieved with the robotic system, and hence the quality of surgery, is highly dependent on the RST capabilities. To provide intuitive manipulation and dexterity enhancement for complex tasks such as suturing, RSTs are commonly equipped with a distal wrist with several (more than two) degrees of freedom (DOF) compared to only two

The associate editor coordinating the review of this manuscript and approving it for publication was Jingang Jiang.

DOF (roll and grasp) found in conventional surgical tools. However, the additional DOF increases the mechanical and control complexity of the device. Various designs of RST have been proposed in the literature [5]. Cable-driven is the most common and preferred form of transmission for RSTs because it allows for compact designs in which the drive actuators can be installed far from the tool wrist, usually at the tool base. In addition, it requires a small number of components and simplifies mechanical construction. EndoWrist instruments are the most widely used RST as they are integrated into the Da Vinci surgical system. EndoWrist instruments have four controllable DOF (pitch, yaw, roll, and grasp) [6]. Other forms of cable-driven surgical instruments with multiple DOF have been proposed in the literature. Thielmann et al. [7] proposed the DLR MICA, a detachable 3-DOF cable-driven RST coupled to a MIRO robot arm for MIS. In [8], Wang et al. designed a cable-driven instrument with a roll-pitch-roll configuration that demonstrated improved performance for suturing and knotting tasks. Chaplin et al. [9] used rotatable pulley arrays to redirect the RST cable. However, the elongation and friction of cables reduce the accuracy of motion and force control and represent an important challenge. Rigid link-based transmission has also been proposed to enhance the structural rigidity of the wrist. Hong and Jo proposed a 3-DOF parallel-linkage design based on a 3-PRS structure [10], while Zhang et al. proposed a serial link mechanism in [11]. The enhanced rigidity of linkage-based RSTs enables high payload capabilities, but they have limited ranges of motion and complex and bulky structures. High power transmission and stiffness can also be achieved with gear-driven tools, as proposed in [12]. An important limitation of the previous approaches is miniaturization, due to constraints imposed by the size of the pulleys, pinned joints, or gears.

Continuum mechanisms are based on intentional elastic structural deformations and have been commonly used for miniaturized medical devices. Francis et al. developed a custom miniaturized continuum instrument for the da Vinci platform [13]. Robert et al. designed a compliant tool based on three-section continuum joints for a single port robotic surgical system [14]. In [15], a lightweight and compact hand-held concentric tube robot was developed and controlled by a user interface located on the tool handle. However, these approaches suffer from low rigidity, low payload capabilities, and low precision. Arata et al. [16] developed a deformable wrist in which elastic strips are used instead of cables to increase rigidity, but the strips are susceptible to early fatigue. The use of superelastic wire-driven surgical instruments has been explored in [17] and [18]. Haraguchi et al. proposed a flexible instrument composed of precision springs and four superelastic wires. Although stiffness is improved, the springs are easily fatigued. Yang et al. also used superelastic wires with snake-like joints and universal joints for a 4-DOF RST. The proposed design showed high payload capabilities and a wide range of motion. Shape memory alloys (SMAs) have also been suggested [19] but exhibit large control delays due to the need for thermal exchange that reduces transparency. Other forms of surgical tools include pneumatic actuators, hydraulic actuators, and magnetic actuators [20]. However, precise motion control is difficult to achieve under such approaches.

From a surgical safety perspective, Kuo et al. suggested that the decoupled motion of the RST joints should be preferred [21]. Furthermore, a decoupled wrist can lead to a simpler control strategy, since each drive motor operates a DOF separately [22] and allows for a direct estimation of the applied forces of each cable tension [23]. On the contrary, EndoWrist instruments have a coupled wrist [4], in which independent control of yaw and pitch angles is not possible, and complex control strategies are used to provide independent motion. Nishizawa and Kishi [24] achieved a decoupled 3-DOF RST by adding an additional joint with a movable rolling contact and a wiring path extended over their contacts. Zhao and Nelson [22] used additional gears and pulleys to decouple the pitch and yaw DOF. Podolsky et al. [25] proposed the use of stationary guide arcs for the design of the wrist of tools. This idea was further explored in [26] and [27]. Jinno [26] proposed a non-interference mechanism to decouple pitch and yaw joints consisting of optimized arc-shaped guides. Chandrasekaran and Thondiyath [27] followed a similar approach but considered a guide rod and the principle of the law of belting in their arc-shaped optimization.

Surgical tools are considered a disposable supply and represent a heavy burden in terms of cost, as most tools are discarded after a few uses [28]. The EndoWrist, for example, is disposed of after 10-15 uses, and considering the high cost and the number and multiple types of tools used in a single RMIS, the total cost per surgery is high. With the current advances in 3D printing, new opportunities have emerged for customized, low-cost surgical instrumentation. However, although it has been extensively used for prototype validation of novel designs, an important limitation for medical applications was the lack of biocompatible materials. Recently, a new range of biocompatible materials has been released, opening new opportunities for 3D-printed devices in surgical environments. We aim to take advantage of the recent progress in biocompatible 3D printing and contribute to the development of RMIS technologies by introducing an open platform for low-cost, biocompatible, and customizable RSTs. The contributions of this work are fourfold.

- A detachable cable-driven RST design with a customizable decoupled end-effector.
- Evaluation of a biocompatible 3D printing material for the development of surgical tools.
- A compact drive unit design and control framework for RSTs.
- Open access to designs and control software for rapid development.

The organization of the paper is as follows. Section II defines the general design requirements for surgical tools.

Section III describes the design, implementation, and control of the proposed RST. We present the experimental validation of the OpenRST performance in Section IV. Finally, conclusions are drawn in Section V.

II. SURGICAL TOOL DESIGN REQUIREMENTS

We define the following requirements that must be considered for an RST design to be used in surgical applications.

A. LOW MANUFACTURING AND MAINTENANCE COSTS

EndoWrist instruments represent a cost of $2000-$5000 per unit [28] and are generally discarded after 10-15 uses since the fatigue of the cable and the pulley increases rapidly with use.

B. STERILIZABILITY AND BIOCOMPATIBILITY

The instruments must be cleaned and sterilized before coming into contact with the human body. Traditional sterilization procedures include plasma and gamma radiation, chemical sterilization (alcohol, ethylene oxide, formaldehyde) and steam sterilization [29], the latter being the fastest and preferred method [30]. Steam sterilization consists of inserting surgical instruments into an autoclave at 132-133 °C, 205 kPa for up to 15 minutes [28]. Robotic surgical instruments, as medical devices, must comply with international standards for biocompatibility (ISO 10993) [31].

C. VERSATILITY

There is an extensive range of tool applications in MIS, and specific design considerations must be specified for each application. Instruments that can be easily adapted for multiple applications are desirable.

D. LOW SIZE AND WEIGHT

In MIS, tools are inserted into the body through a cylindrical port (trocar) or natural orifices with diameters between 5-10 mm [32]. The external diameter of the tool is expected to be reduced to minimize the size of the incision and avoid disruptions inside the patient's body.

III. OpenRST DESIGN

Based on the above design requirements, we present an RST design concept consisting of three main components: a customizable 3-DOF end-effector with a decoupled wrist mechanism, a detachable tool interface module, and a tool drive unit.

A. OpenRST END-EFFECTOR

1) DECOUPLED WRIST MECHANISM

The wrist mechanism is designed to provide 3-DOF: pitch, yaw, and grasp. It features a motion range of ±90° for the pitch axis (θ_p) and the yaw axis (θ_y). The grasping motion θ_g is achieved by adding an offset from the desired θ_y to each jaw joint. Roll motion has not been considered as the RST can be attached and aligned to a robot manipulator end-effector

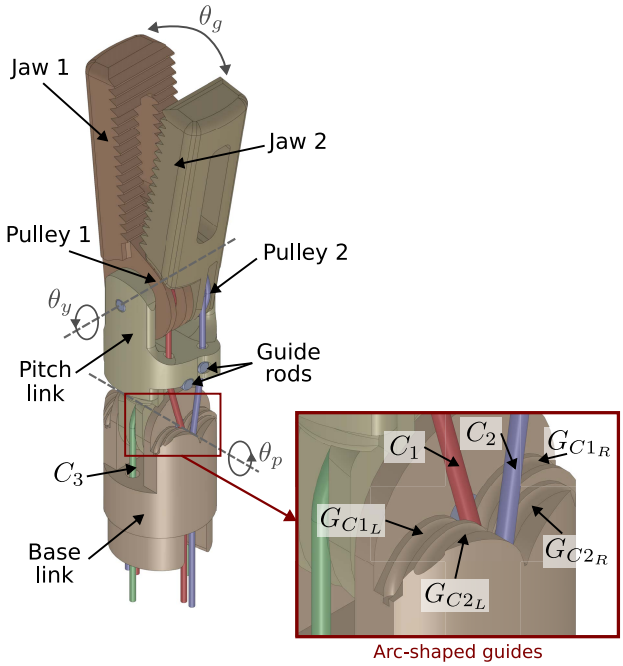

FIGURE 1. CAD illustration of the decoupled wrist link. In the close-up view, one side of the arc-shaped guides for C_1 and C_2.

joint axis and get direct control over the roll motion. Decoupled wrists can simplify the RST control strategy and allow for independent torque transmission. The computer-aided design (CAD) model of the proposed end-effector is shown in Fig. 1. Cable transmission is chosen because it can achieve long-distance transmission in small spaces. Three cables denoted C_1, C_2, and C_3 actuate the two jaw joints and the pitch joint, respectively. Cables C_1 and C_2, colored red and blue, respectively, pass through internal channels in the base link to reach the jaw pulleys. As the distances between the entry/exit holes in the base link are different for the cables C_1 and C_2, the diameter of the jaw pulleys also differs, with the diameter of jaw pulley 2 being larger than the diameter of jaw pulley 1. This helps prevent cables from sliding off the pulleys and increases the useful life of the tool [27]. Additional guide rods placed on the pitch link align the center of the incoming cable with the jaw pulleys' midplane.

A total of eight arc-shaped guides are added to the base link to ensure a smooth trajectory of the jaw cables during any pitch angle. Figure 1 includes a close-up view of one side of the base link in which four of the solid arc-shaped guides designed to guide C_1 and C_2 are visible. There are two arc-shaped guides, G_{C1_L} and G_{C1_R}, for the left and right sides of C_1, respectively, and two arc-shaped guides G_{C2_L} and G_{C2_R} for C_2. The use of these guide arcs allows for a decoupled movement of the jaw joints with respect to the pitch joint and leads to a reduction in the number of components, simplifying manufacturing, reducing costs, and prolonging useful life [25].

Ideal guides should not create any deformation of the cable. However, since the centers of the guides have an offset

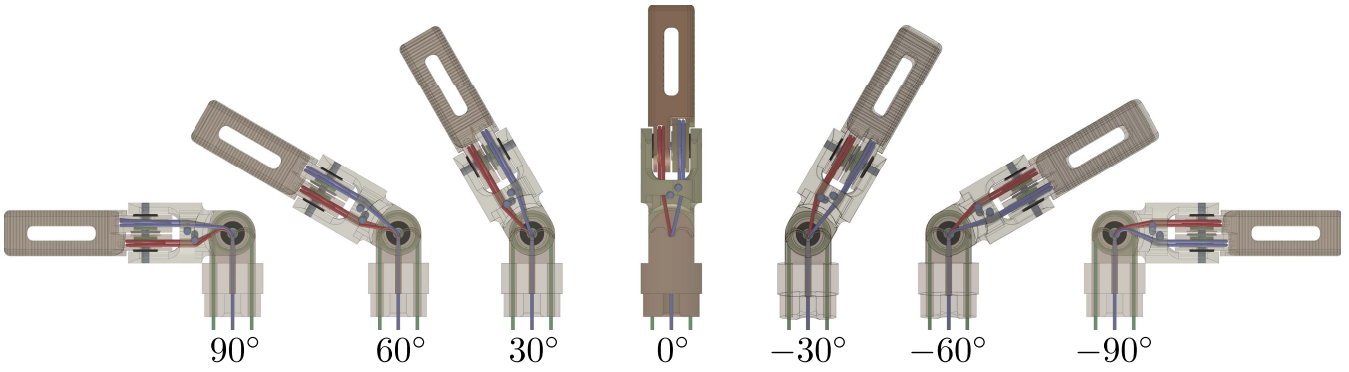

FIGURE 2. Change in cable length at multiple pitch angles.

relative to the center of pitch rotation and the flexibility of the cables is limited, they still suffer from stretching or slackening at different pitch angles. Figure 2 presents a CAD illustration of the end-effector at different pitch angles showing the changes in cable length for C_1 and C_2 when following the arc-shaped guides. The extent of cable deformation will highly depend on the location and dimensions of the arc-shaped guides, and therefore an optimized design is required.

2) OPTIMIZATION OF THE ARC-SHAPED GUIDES

The design of the arc-shaped guides should be optimized to minimize cable deformation when the pitch link rotates around the pitch angle θ_p. As C_1 and C_2 are antisymmetrical, here we present only the analysis for C_1 by optimizing G_{C1_L} and G_{C1_R}. The corresponding optimized parameters for C_2 can be obtained as mirror images of G_{C1_L} and G_{C1_R}.

The reference frame is centered at O, coincident with the pitch rotation axis. The pitch joint θ_p has a range of $[-90°, 90°]$ with zero defined when the pitch link aligns with the base link. The optimization problem can be divided into two subproblems depending on the region where the cable is located:

- Left quadrant region ($\theta_p > \theta_{thresh}$): The cable C_1 turns around the guide G_{C1_L}, and
- Right quadrant region ($\theta_p < \theta_{thresh}$): The cable C_1 turns around the guide G_{C1_R}.

The threshold angle θ_{thresh} represents the angle under which C_1 transfers from G_{C1_L} to G_{C1_R}, that is, the cable does not rest on either arc-shaped guide.

Figure 3 represents the first case where the cable C_1 is in contact with the left cable guide G_{C1_L}. The cable follows the circumference ζ_1 from the point a to the point b, with the inscribed angle represented by ϕ_1 and the subtend arc denoted $\widehat{ab}$. The cable leaves G_{C1_L} at b and comes into contact with the guide rod at c. The line segment tangent to both circumferences ζ_1 and ζ_2 is represented as $\overline{bc}$. The cable then turns around the guide rod following the arc $\widehat{cd}$, aligning the cable with the jaw pulley and leaving the guide rod at d. The segment $\widehat{ad}$, represented in green, is the only cable section that suffers from length changes when the wrist pitches.

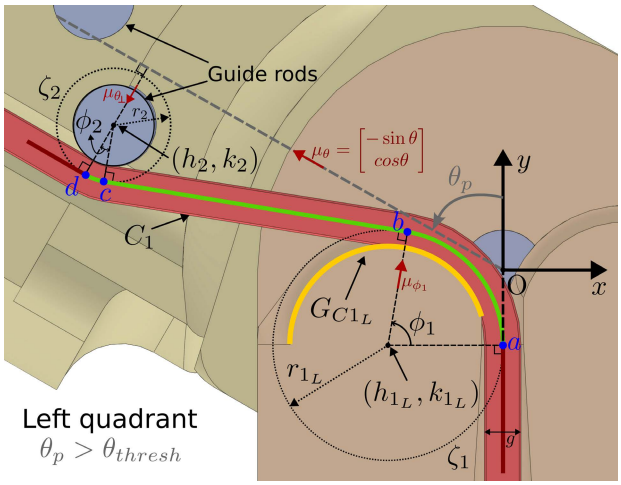

FIGURE 3. Cable C_1 in the left quadrant guided by the left arc-shaped guide G_{C1_L}.

Therefore, our focus is only on reducing length variations along this segment.

The length of the segment $\widehat{ad}$ is defined as the sum of the length of the tangent line $\overline{bc}$ and the arc lengths of $\widehat{ab}$ and $\widehat{cd}$. The y-axis offset between the left and right guide arcs is also added when $k_{1_L} > k_{1_R}$:

$$\ell_{C1_L} = r_{1_L}\phi_1 + \overline{bc} + r_2\phi_2 + |\min(0, h_{1_R} - h_{1_L})|. \quad (1)$$

The inscribed angle ϕ_2 and the coordinates of b and c can be expressed as a function of the center coordinates of $\zeta_{1_C} = (h_{1_L}, k_{1_L})$ and $\zeta_{2_C} = (h_2, k_2)$, the circumference radius r_1 and r_2, the pitch angle θ_p and the inscribed angle ϕ_1. The coordinates of b can be obtained directly as

$$\begin{bmatrix} b_x \\ b_y \end{bmatrix} = \begin{bmatrix} h_{1_L} \\ k_{1_L} \end{bmatrix} + r_1\mu_{\phi_1} = \begin{bmatrix} h_{1_L} \\ k_{1_L} \end{bmatrix} + r_1 \begin{bmatrix} \cos\phi_1 \\ \sin\phi_1 \end{bmatrix}. \quad (2)$$

From the geometrical relations shown in Fig. 3, the coordinates of c can be computed as

$$\begin{bmatrix} c_x \\ c_y \end{bmatrix} = \begin{bmatrix} h_2 \\ k_2 \end{bmatrix} - r_2\mu_{\phi_1} = \begin{bmatrix} h_2 \\ k_2 \end{bmatrix} - r_2 \begin{bmatrix} \cos\phi_1 \\ \sin\phi_1 \end{bmatrix}. \quad (3)$$

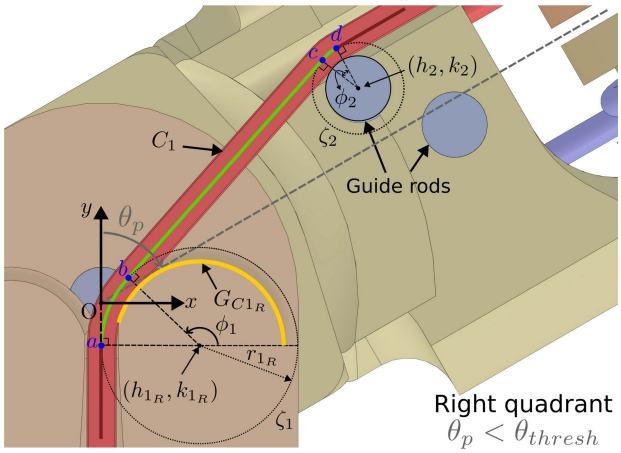

FIGURE 4. Cable C_1 in the right quadrant guided by the right arc-shaped guide G_{C1_R}.

The center of ζ_2 changes with θ_p and can be computed as

$$\begin{bmatrix} h_2 \\ k_2 \end{bmatrix} = \begin{bmatrix} -k_{2_0} \sin\theta_p + h_{2_0} \cos\theta_p \\ k_{2_0} \cos\theta_p - h_{2_0} \sin\theta_p \end{bmatrix}, \tag{4}$$

with h_{2_0} and k_{2_0} denoting the initial coordinates of the center of ζ_2 when $\theta_p = 0$.

Finally, the inscribed angle ϕ_2 can be calculated as

$$\phi_2 = \phi_1 - \theta_p. \tag{5}$$

The points b and c belong both to the tangent line $\overline{bc}$ and to the circumferences ζ_1 and ζ_2, respectively. By solving the system of equations (see Appendix V), the following expression is obtained for ϕ_1.

$$\phi_1 = -2 \arctan\left(\frac{k_{1_L} - k_2 + \sqrt{M}}{h_2 - h_{1_L} + r_{1_L} + r_2} \right) \tag{6}$$

with $\mathrm{M} = (h_{1_L} - h_2)^2 + (k_{1_L} - k_2)^2 - (r_{1_L} + r_2)^2$.

For the right quadrant case, shown in Fig. 4, the length of the segment $\widehat{ad}$ can be expressed in a similar way as follows.

$$\ell_{C1_R} = r_{1_R}(\pi - \phi_1) + \overline{bc} + r_2\phi_2 + |\min(0, h_{1_L} - h_{1_R})| \tag{7}$$

The points b and c can be found following the same approach as for the left arc guide. The coordinates for b are the same as in (2), and the coordinates for c can be expressed as

$$\begin{bmatrix} c_x \\ c_y \end{bmatrix} = \begin{bmatrix} h_2 \\ k_2 \end{bmatrix} + r_2 \begin{bmatrix} \cos\phi_1 \\ \sin\phi_1 \end{bmatrix} \tag{8}$$

The inscribed angle ϕ_2 is then calculated as

$$\phi_2 = \phi_1 - (\pi + \theta_p). \tag{9}$$

Solving again the system of equations for ϕ_1 we obtain

$$\phi_1 = -2 \arctan\left(\frac{-k_1 + k_2 + \sqrt{N}}{h_1 - h_2 - r_1 + r_2} \right) \tag{10}$$

with $\mathrm{N} = (h_{1_R} - h_2)^2 + (k_{1_R} - k_2)^2 - (r_{1_R} - r_2)^2$.

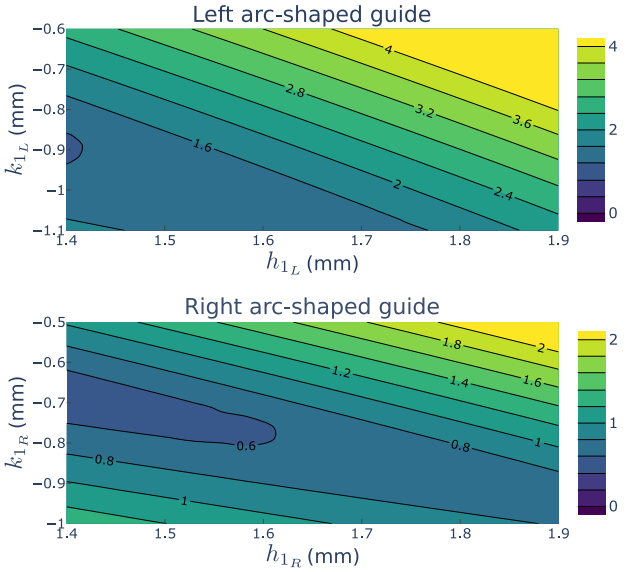

FIGURE 5. Optimization search.

We consider the arc-shaped guides to be tangential to the symmetry line and assume that $h_{1_L} = -r_{1_L}$ and $h_{1_R} = r_{1_R}$. Furthermore, to reduce the deformation caused by the guide rods, r_2 should be small, while k_2 should be large. For manufacturing purposes, the guide rods used have a diameter of 1 mm ($r_2 = 0.725$ mm) and are placed with $k_{2_0} = 5$ mm for C_1 and $k_{2_0} = 6$ mm for C_2. The value of h_{2_0} is obtained as $h_{2_0} = lp - r_2$, where lp represents the distance of the jaw pulley midplane from O. A 7×7 stainless steel cable with diameter $g = 0.45$ mm was chosen to provide enough flexibility and load force. Cable-driven RSTs usually have a high curve ratio, with the EndoWrist having a curve ratio of 5:1 [33]. A minimum bending curve ratio of 6.5:1 is considered to avoid damaging the cable while maintaining a compact design. The variables to be optimized and the search domain are defined as $r_1 \in [1.4\text{ mm}, 2.5\text{ mm}]$ and $k_1 \in [-2.0\text{ mm}, 0\text{ mm}]$.

The cable pretension by the driving drums is performed with $\theta_p = 0$. The reference segment length is defined as $\ell_{ref} := \{\ell_{C1} | \theta_p = 0\}$. Our aim is to minimize cable deformation with respect to the reference segment length ℓ_{ref}. An objective function to be minimized can then be defined as:

$$J(r_{1_{[n]}}, k_{1_{[n]}}, \theta_{p_{[n]}}) = \Delta\ell_{max} + \Delta\ell_{rms} \tag{11}$$

where $\Delta\ell_{max} := \max(|\ell_{[n]} - \ell_{ref}|)$ and $\Delta\ell_{rms} := \sqrt{\frac{1}{N}\sum(\ell_{[n]} - \ell_{ref})^2}$ with N representing the number of step points in the pitch joint range.

An exhaustive grid search was performed to find the optimal values. The pitch angle θ_p is discretized in 50 steps that range from $[-1.57\text{ rad}, 1.57\text{ rad}]$, and the search space for r_1 and k_1 is also discretized in 25 steps.

Figure 5 shows the contour plots for the optimization search, with the color representing the value of the objective

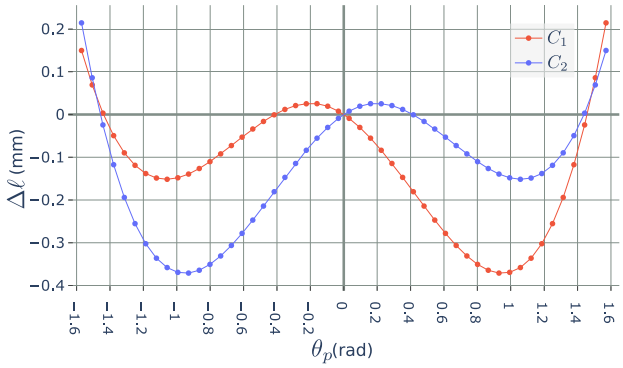

FIGURE 6. Optimized theoretical cable deformation for C_1 and C_2.

TABLE 1. BioMed Amber Resin Specifications.

Property	Value
Tensile Strength	73 MPa
Young's Modulus	2.9 GPa
Flexural Strength	103 MPa
Flexural Modulus	2.5 GPa

function for a given (h_1, k_1). The top graph represents the values of the objective function for the arc-shaped guide on the left. The optimized values were found to be in $(h_{1_{L_{opt}}}, k_{1_{L_{opt}}}) = [1.4, -0.9]$. The search for the right arc guide is shown below, and the optimized values were selected as $(h_{1_{L_{opt}}}, k_{1_{L_{opt}}}) = [1.5, -0.7]$.

The optimized theoretical deformation for each cable with respect to the reference length ℓ_{ref} along the pith joint range of motion θ_p is shown in Fig. 6. The maximum deformation under optimal values corresponds to 0.38 mm.

3) MANUFACTURING

3D printing provides a low-cost customizable solution for the development of surgical tools. However, an important limitation is the lack of biocompatible and sterilizable materials. Furthermore, the material should have high strength and stiffness characteristics to avoid bending or breaking during surgery. To meet these requirements, we chose BioMed Amber Resin (Formlabs) [34]. BioMed Amber Resin is a biocompatible material that has been evaluated with ISO-10993-1: 2018 for the biological evaluation of medical devices and complies with ISO Standards 13485: 2016 and ISO 14971: 2012. This material can be sterilized by autoclave, E-beam, gamma, and ethylene oxide. Table 1 summarizes the main properties of the material.

The Da Vinci RST, EndoWrist, can reach grip forces of up to 20 N [35] with a mean grip force of 15 N [36]. However, a maximum grip force of 4 N and 10 N has been suggested to avoid tissue damage [37] and break sutures [38]. Therefore, we expect our end-effector to meet a grip force range of [0 N, 10 N].

We validate our end-effector design with Finite Element Analysis (FEA) to confirm that the maximum grip force that can be applied keeps the predicted stress below the material yield stress. Figure 7 shows the FEA stress results for a Fenestrated end-effector jaw link when 16 N is applied at the center of the jaw.

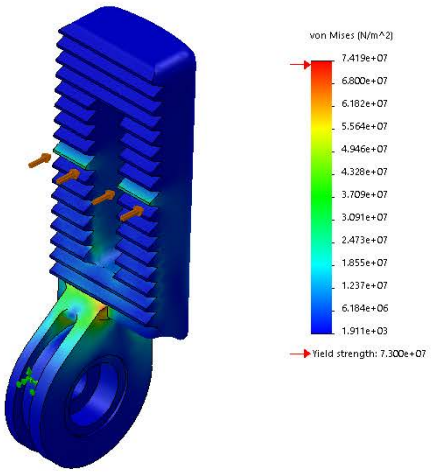

FIGURE 7. FEA analysis showing stress for a single end-effector jaw link at the maximum expected force (16N) applied at the center.

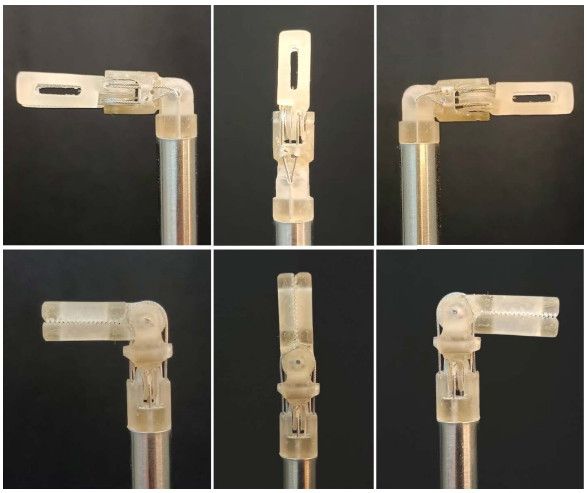

FIGURE 8. Assembled 3D printed Fenestrated end-effector. At the top, the end-effector rotates around the pitch axis. At the bottom, it rotates around the yaw axis. In all images, the jaws are kept closed.

Our proposed open platform for RST allows replacing the Fenestrated jaw link design with other surgical end-effector types or even custom designs for specific surgical applications. We provide some examples of other end-effectors including Maryland, Needle driver, and Scissor end-effector types. FEA analysis with these designs was carried out to verify that the maximum stress generated within the desired force range is below the material yield stress. Table 2 shows the maximum forces to be applied in the center and at the end of each type of end-effector according to the FEA analysis.

The end-effectors are 3D printed using a Form 2 SLA 3D Printer (Formlabs) with BioMed Amber Resin (Formlabs). After printing, the parts were washed for 15 minutes in IPA

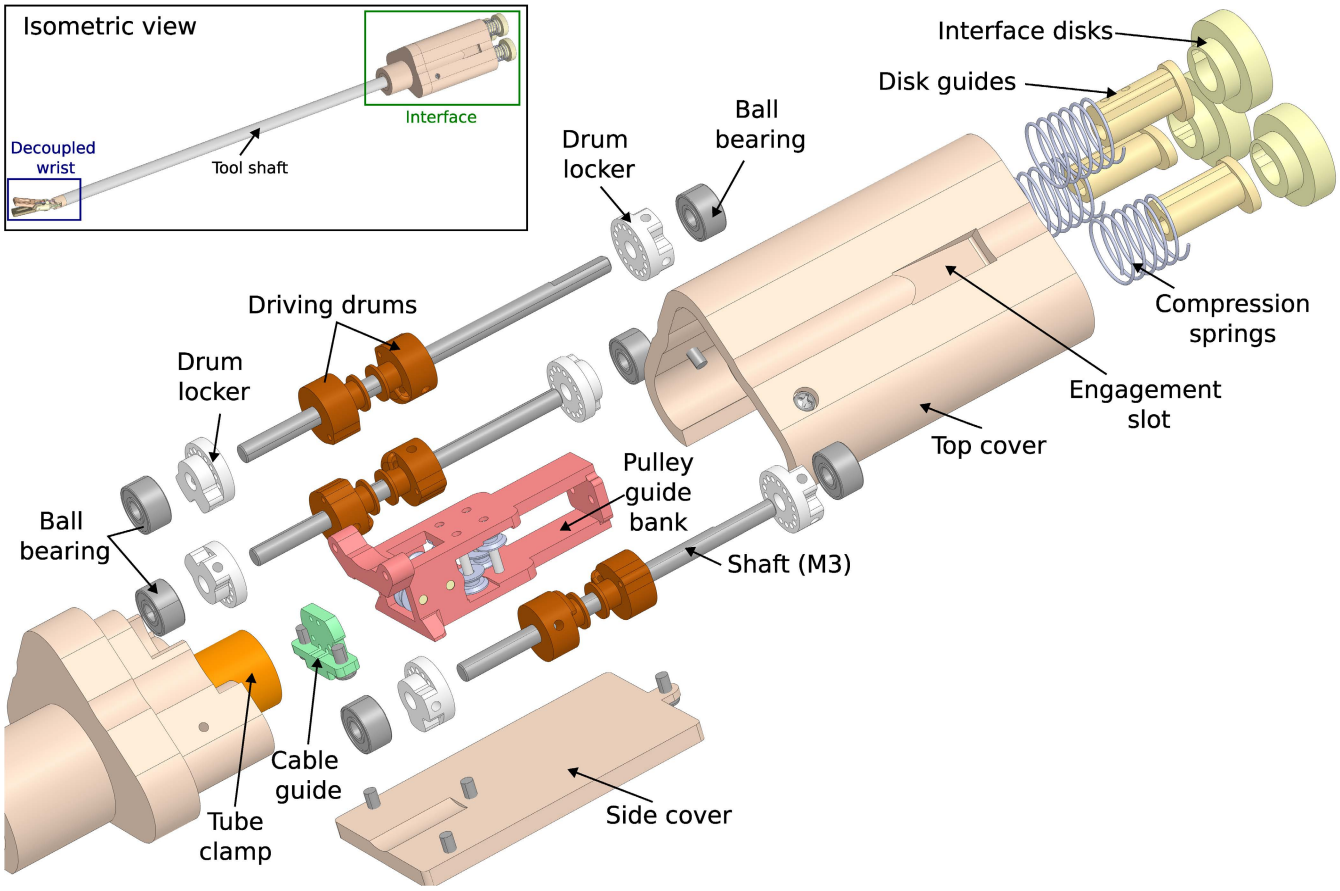

FIGURE 9. Exploded view of the OpenRST interface module. The tool shaft works as a link connecting the interface module with the decoupled wrist end-effector.

TABLE 2. Maximum forces for different types of OpenRST tips.

End-effector type	Max. Force at the tip (N)	Max. Force at the center (N)
Fenestrated	10	16
Maryland	10	16
Needle Driver	14	20
Scissor	10	16

and cured under UV light for one hour. The assembled fenestrated end-effector is shown in Figure 8. The upper images show the jaws closed at 0° and the pitch joint rotated at −90°, 0° and 90°. The bottom images show the jaws closed and the yaw joint rotated at −90°, 0°, and 90°.

B. OpenRST INTERFACE MODULE

1) INTERFACE DESIGN

Each distal DOF is controlled by a capstan drive mechanism composed of two driving drums mounted on a rotating shaft. The ends of the cable are winded and fixed on the driving drums. The cable travels starting from one drum through a train of guide pulleys, passing through a cable guide to reach the jaw pulley, and returning in the same way to the other driving drum. The drums are fixed to the shaft with set screws, and the fixture is reinforced with a drum locker by inserting

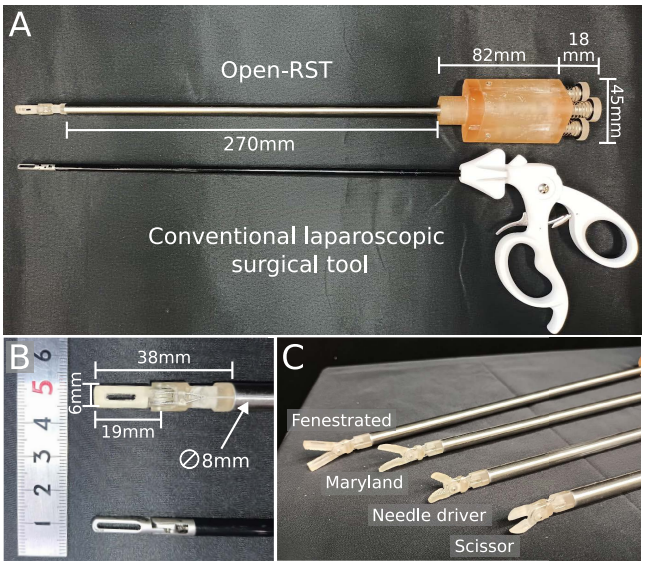

FIGURE 10. A. OpenRST interface module dimensions. B. Fenestrated end-effector dimensions C. Set of different end-effectors types printed.

a pin that passes through both a drum lock and the driving drum. If a change in cable pretension is needed, the pin can

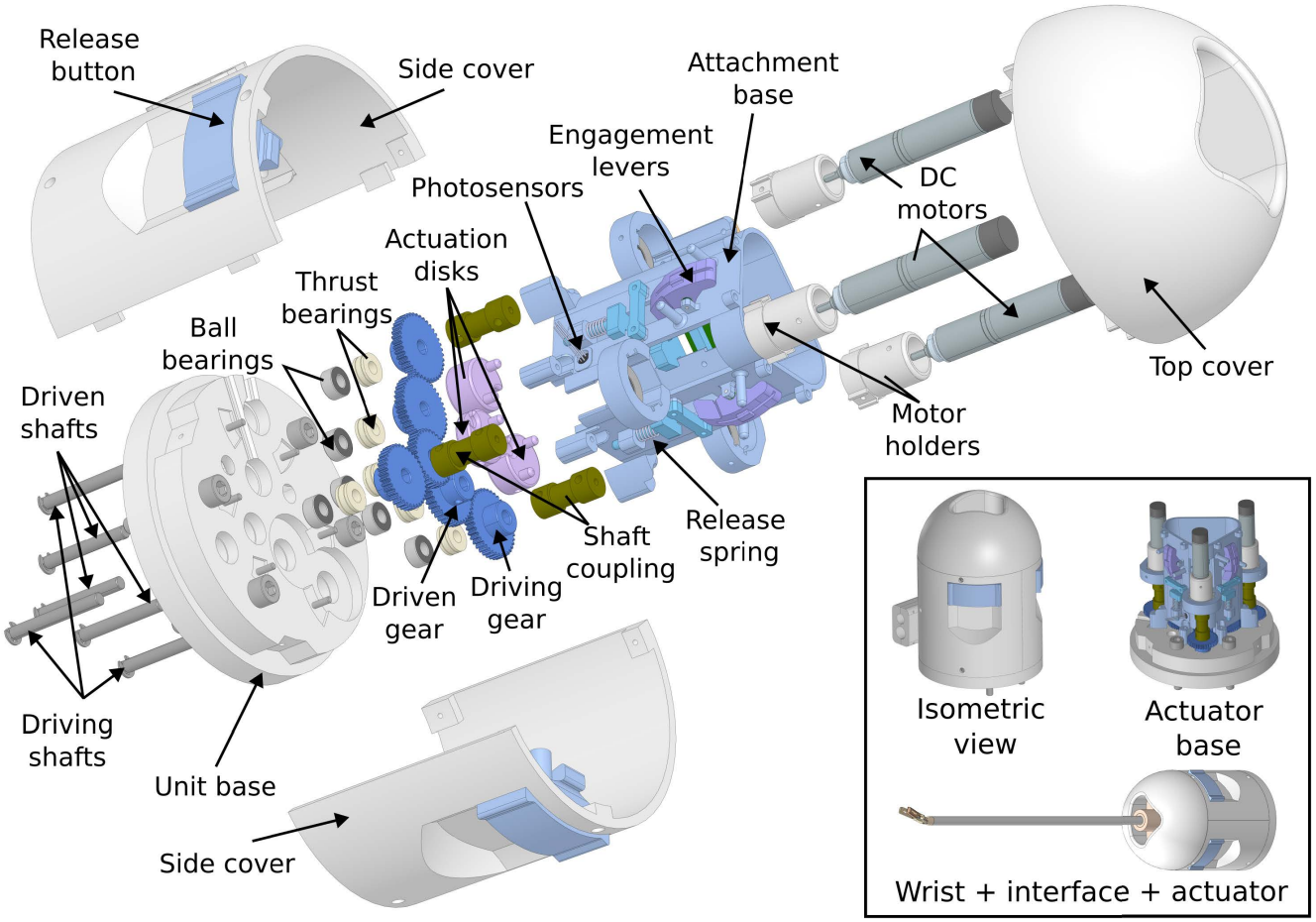

FIGURE 11. Exploded view of the OpenRST drive unit.

be removed and the drum set screws lose. The drums can then be rotated in opposite directions until the desired pretension is achieved, and then fixed by locking the set screws and inserting the lock pin again. A pulley guide bank containing 6 pulleys (2 for each DOF) reorients the cable towards the end-effector. At the end of each rotating shaft, a disk guide is attached. Three interface disks are mounted on each disk guide, with free movement only along the longitudinal axis of the guide. Each interface disk has two circular notches placed symmetrically for engagement with the actuation disk of the driving unit. Compression springs are inserted between the guide bases and the interface disks to allow the latest to retract when the notches do not match with the protrusions in the actuation disks. After calibration, both disks are aligned, and the compression springs keep the interface disks fixed against the actuation disk. An exploded view of the RST interface CAD design is shown in Figure 9.

The cables travel from the tool interface to the decoupled wrist mechanism through a stainless steel shaft. The interface structure is printed with the same biocompatible material BioMed Amber Resin in a Form 2 SLA 3D Printer (Formlabs). The final dimensions of the OpenRST tool are shown in Fig. 10. The tool interface module has a triangular shape with a length of 100 mm and a width of 45 mm. For a fenestrated end-effector, the total length is 308 mm, which is similar to the length of a conventional laparoscopic surgical tool. The diameter of the tool is 8 mm, which facilitates its insertion through surgical trocars.

C. OpenRSt DRIVE UNIT

1) DRIVE UNIT

The actuator unit comprises three compact brushless DC motors (RE10 1.5W ∅10 mm, Maxon), each controlling a distal DOF with a maximum supply torque of 3mNm. For the pitch joint, a planetary gear (GP10A, Maxon) with a reduction ratio of 1:256 was used, while for the jaw joints, a planetary gear (GP10A, Maxon) with a reduction ratio of 1: 64 was selected. Each motor contains an incremental encoder with a resolution of 16CPT. Motors are placed on each side of the attachment base to reduce the moment of inertia of the drive unit. Each motor is mechanically coupled to a drive shaft with a driving gear, which meshes with a driven gear to rotate the actuation disk. The gear ratio between the driving and driven gears is 40:40 for the jaw joints and 36:32 for

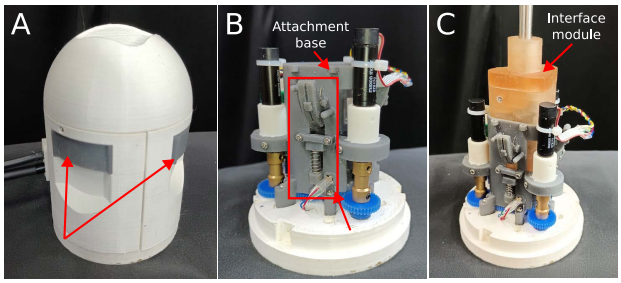

FIGURE 12. OpenRST Drive unit. A. Covers are attached and the release buttons are visible. B. The covers are removed and the attachment base with the engagement mechanism is visible. C. Drive unit with the interface module engaged.

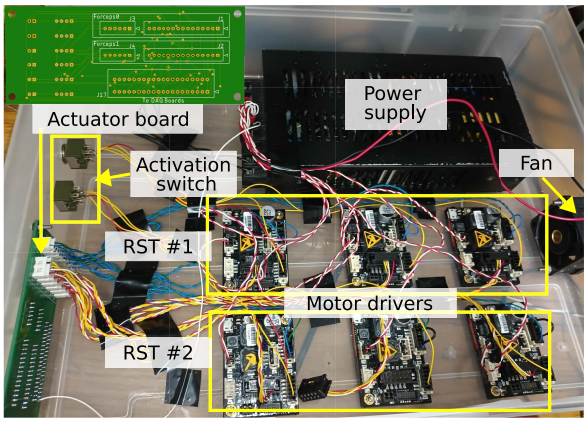

FIGURE 13. Controller Box designed for two OpenRSTs.

the pitch joint. Each actuation disk contains two cylindrical protrusions placed equidistantly from the disk center that mate with the interface disk notches. The drive unit control board is mounted on one side of the attachment base and acts as an interface for the sensors and actuators of the drive unit with the controller box. An exploded view of the drive unit is presented in Fig. 11.

The actuator unit is not intended to be in direct contact with the patient and therefore does not need to be manufactured with a biocompatible material. To provide high durability, the attachment base is printed with Tough 2000 Resin (Formlabs) on a Form2 SLA 3D printer (Formlabs) and the unit base and covers with PLA on an Ultimaker 3+. Figure 12 shows the assembled drive unit with and without covers for better visualization of the attachment base.

2) TOOL EXCHANGE MECHANISM

A key consideration in OpenRST design is fast and easy instrument interchangeability. The tool interface is inserted into the drive unit through the triangular profile of the attachment base. Two engagement levers located on the sides of the attachment base contain torsion springs that keep the flat end of the levers inside the attachment cavity. The levers retract when in contact with the flat area of the interface cover and engage with the tool interface engagement slots to prevent it from being released. Three release springs located on each side of the attachment base press the interface slots against the flat surface of the levers to fix the position of the interface module and provide a release force to eject the interface when the engagement levers are pressed at the opposite end by the release buttons. This engagement mechanism allows for quick tool insertion and extraction by simply pressing the engagement cams. To verify disk engagement, three photosensors (SG-2BC, Kodenshi Corp.) are placed in the attachment base above the actuation disk to detect the presence of the interface disk.

3) CALIBRATION

Each tool could require a different calibration. After a new tool is engaged in the drive unit, a calibration procedure is performed as follows: i) Each of the interface plates rotates independently until the corresponding photosensor detects the interface disks engaged with the actuation disks. ii)The pitch joint rotates clockwise. When the motor current reaches a predefined threshold, it is assumed that the joint reached the joint limit and the encoder value is recorded. iii) The pitch joint rotates counterclockwise until it reaches a motor current threshold. The encoder value is then recorded. iv) The pitch joint is positioned at the center for the calibration of the jaw joints. v) Steps ii-iv are repeated for the calibration of each jaw joint. vi) Once the calibration is completed, the servo control is enabled.

4) CONTROLLER ARCHITECTURE

Each motor is controlled by a DC motor driver (ESCON 36/2 DC, Maxon). A total of three motor drivers are needed for one drive unit. The drive unit contains a control board placed on one side of the attachment base and communicates with a controller box. A controller box was designed for the simultaneous control of two OpenRST units (shown in Fig. 13). Each motor driver receives a desired current command as an analog voltage input from a data acquisition (DAQ) board (USB3104, Measurement Computing). Motor encoder signals are received by a counter DAQ board (USBQUAD08, Measurement Computing), and photosensor signals and motor current signals are read from an analog input DAQ board (USB1604, Measurement Computing).

5) ROS CONTROL PACKAGE

The OpenRST control is implemented using the Robot Operating System (ROS) framework with a control frequency of 500Hz. Two packages are provided with the OpenRST platform:

- mc_daq_ros: Node handling communication with the USB DAQ boards.
- openrst_control: The main control node. It uses the ROS-control package [39] in its core. Receive the target joint positions θ_{des} and generate a voltage command v_cmd for each DOF of the tool. Update current joint positions based on encoder readings.

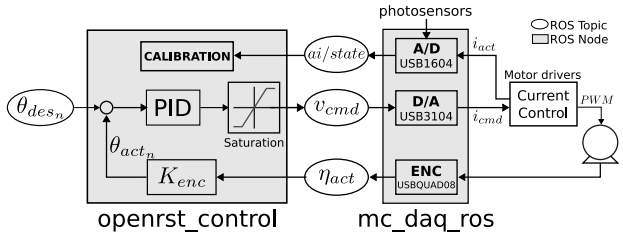

FIGURE 14. Controller framework. A target position θ_{des} is the input for the open_rst_control node. A PID controller generates v_{cmd}, which is received by the mc_daq_ros node to generate an analog input command for the motor drivers. The encoder signal is obtained from the mc_daq_ros node and sent to the open_rst_control for the generation of a new command.

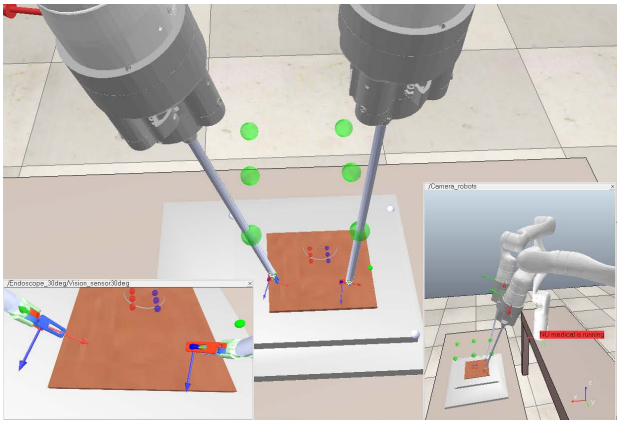

FIGURE 15. Simulation of two OpenRST attached to two robotic manipulators in CoppeliaSim. The URDF files were used to create the simulation models.

The ROS control architecture is shown in Figure 14.

A Unified Robot Descriptive Format (URDF) containing the kinematic description of the OpenRST is also provided. It allows for easy integration into robotic kinematic libraries and simulation environments. Figure 15 depicts the URDF model deployed in a CoppeliaSim environment [40].

IV. EXPERIMENTAL VALIDATION

Performance validation of the proposed RST was carried out by evaluating maximum grip and pull forces, torque transmission efficiency, position tracking accuracy, and demonstrating the use of OpenRSTs in surgical training tasks.

A. GRIP FORCE ANALYSIS

The experimental setup is shown in Fig. 16A. An OpenRST drive unit with the inserted interface module is attached to a fixed base. For these experiments, a fenestrated end-effector type is used.

1) GRIP FORCE

The maximum grip force was obtained by applying a normal force over a force/torque sensor (Nano17, ATI Industrial Automation). One of the jaws is kept at a fixed open angle,

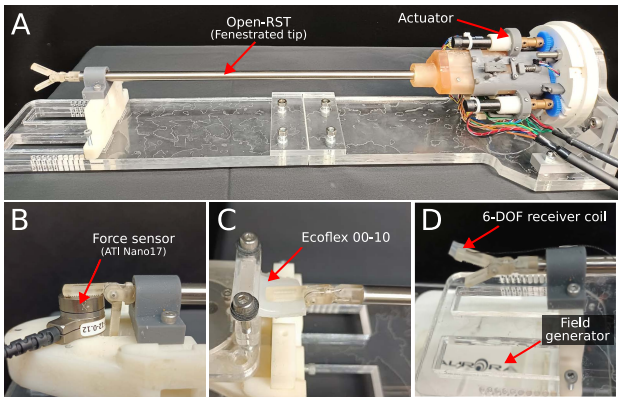

FIGURE 16. Experimental setup. A. OpenRST drive unit with a fenestrated end-effector and interface module inserted. B. A force sensor is placed in contact with one jaw link to measure the grip force. B. An silicone phantom is used to measure pull-out strength. C. A magnetic receiver coil sensor is attached to the end-effector tip to record the angle of the yaw joint.

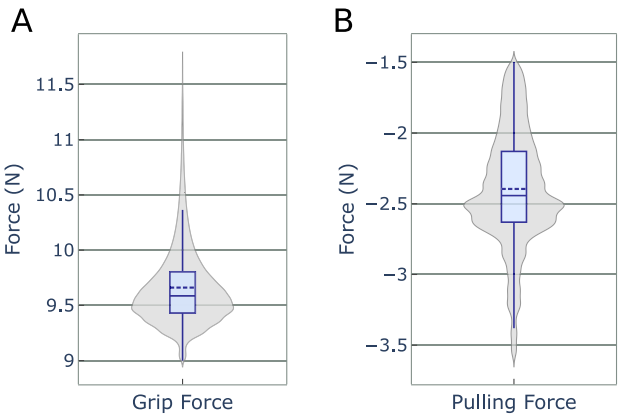

FIGURE 17. A. Grip force results. B. Pull-out strength force.

while the other jaw is controlled to press and release a normal force against the sensor. The task is repeated 50 times and the maximum forces are registered. The results are shown in Fig. 17A. The violin plot shows a mean maximum grip force of 9.6N with peaks of up to 11N. The results are within the optimal force range suggested for MIS of 10N [41].

2) PULL OUT STRENGTH

To measure the pull-out strength, a silicon phantom is used to represent soft tissue. The silicone material used was EcoFlex 00-10 with a shore hardness of 00-10. The sample is attached to a force sensor (Mini40, ATI Industrial Automation) that can be moved only on the longitudinal tool axis. The sample is grasped with both jaws and the pitch angle at $0/circ$. Once the sample is grasped, the force sensor base is pulled in the opposite direction of the actuator until the sample is released from the jaws. The maximum force is recorded. The task was repeated 50 times. The results are shown in Fig. 17B. The violin plot shows a mean pulling force of 2.4N.

TABLE 3. Torque Transmission Efficiency at Maximum Grip Force.

τ_{meas} (mNm)	τ_{est} (mNm)	Efficiency η (%)
91.2	98.5	92.5

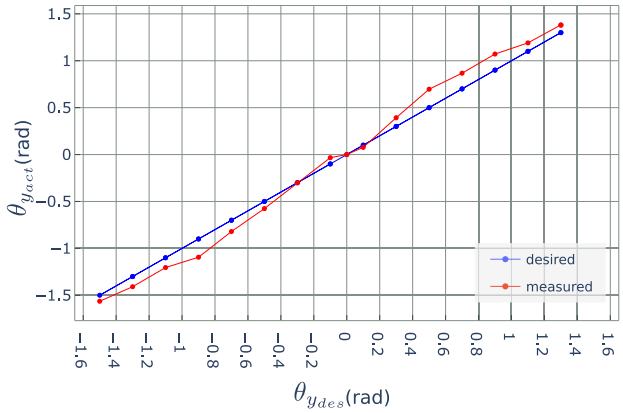

FIGURE 18. Yaw joint angular positioning accuracy. The blue line represents the target angle, and the average measured angle obtained from the motion tracker is represented in red.

B. TORQUE TRANSMISSION EFFICIENCY

We evaluated the torque transmission efficiency, defined as the relation between the measured tooltip torque and the theoretical torque transmitted to the tooltip as follows:

$$\eta = \frac{\tau_{meas}}{\tau_{est}} = \frac{f_{g_{mean}} d_g}{\tau_m \frac{r_d}{r_g}} \tag{12}$$

where $f_{g_{mean}}$ represents the mean maximum grip force from Section IV-A1, d_g represents the distance from the center of the Fenestrated tip to the jaw joint, r_d is the radius of the drive drum pulley, r_g is the diameter of the jaw pulley and τ_{est} is the theoretical transmitted torque approximated as a function of the driving motor current $\tau_m = k_\tau \mathcal{I}_{act} N_m N_g$, k_τ is the motor current coefficient, $\mathcal{I}_{act}$ is the actual motor current measured from the motor driver, N_m is the motor gear reduction ratio and N_g denotes the gear ratio of the actuation disks. For the motors selected $k_\tau = 4.56$ mNm/A, $N_m = 64:1$, and $N_g = 40:40$. When applying the maximum grip force, the measured current corresponds to $\mathcal{I}_{act} = 0.33$ A. The torque transmission efficiency obtained is 92%.

C. ANGULAR POSITIONING ACCURACY

To evaluate the accuracy of the angular positioning of the proposed controller, a magnetic motion tracker (Aurora, Northern Digital Inc.) is used. A 6-DOF receiver coil sensor is attached to the tip of one of the jaws and the field generator is placed below the tooltip. Target position commands are then sent to the end-effector and the measured tip pose is recorded. The target angles are uniformly distributed and range from −1.5 rad to 1.5 rad. The angular positioning error θ_{err_k} is calculated as the difference between the target angle $\theta_{y_{des_k}}$ and the actual angle $\theta_{y_{act_k}}$. The task was repeated 10 times. Figure 18 shows the desired target angle in blue and the average of the measured angles in red. It can be observed that the tracking error is low in the region close to the center (0°) and larger at the extremes of the yaw range of motion (±90°).

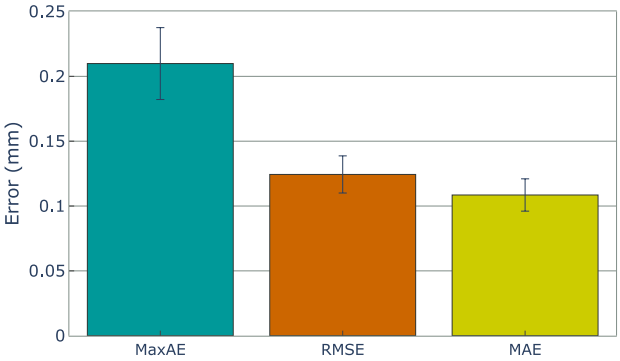

FIGURE 19. Angular tracking error.

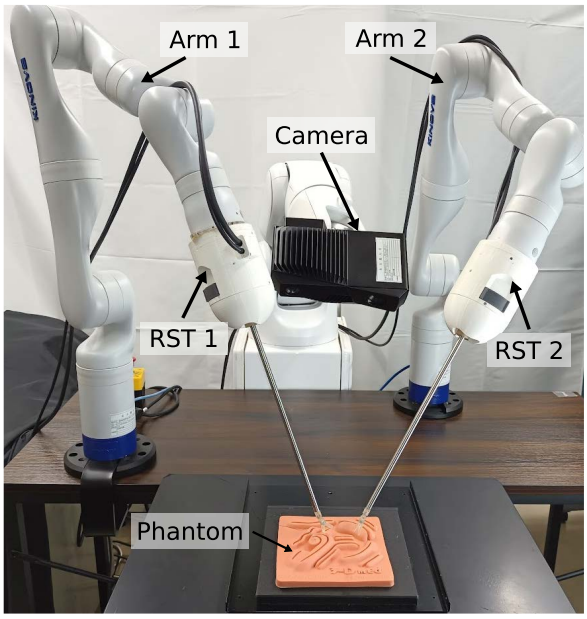

FIGURE 20. OpenRST attached to robot arms for usability demonstration of the proposed OpenRST in surgical tasks.

For each trial, the following tracking errors were calculated:

- Maximum Absolute Error (MaxAE):

$$\max_{k \in K} \{ |\theta_{y_{act_k}} - \theta_{y_{des_k}}| \} \tag{13}$$

- Root Mean Squared Error (RMSE):

$$\sqrt{\frac{1}{K} \sum_{k}^{K} (\theta_{y_{act_k}} - \theta_{y_{des_k}})^2} \tag{14}$$

- Mean Absolute Error (MAE):

$$\frac{1}{K} \sum_{k}^{K} |\theta_{y_{act_k}} - \theta_{y_{des_k}}| \tag{15}$$

The bar graphs in Fig. 19 summarize the results obtained. The mean MaxAR for all trials was 0.21 rad, the mean

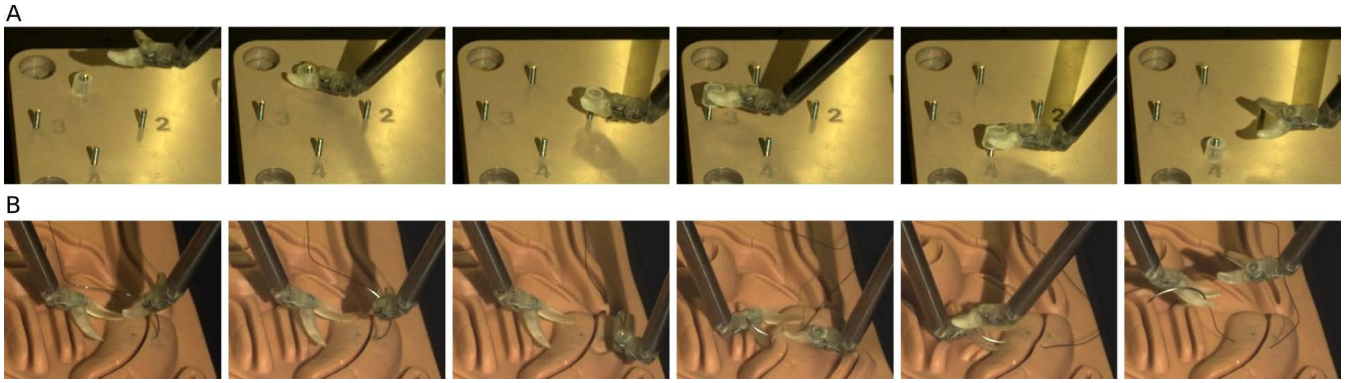

FIGURE 21. Snapshots of OpenRSTs performing surgical training tasks: A. Pick and place task. B. Stitching.

RMSE obtained was 0.12 rad, and the MAE obtained was approximately 0.11 rad.

D. SURGICAL TASK

The use of the proposed RST is demonstrated in two common surgical training tasks: pick-and-place and stitching. Two OpenRSTs are attached to a robotic manipulator each (7-DOF Gen3, Kinova). The manipulators and forceps are controlled simultaneously and teleoperated by a haptic interface (Touch, SensAble Technologies) with no force feedback. The interface tip pose commands the RST end-effector pose. A virtual RCM is implemented in robot motion planning control to resemble the constraints imposed by trocars in MIS [42].

Figure 21 presents snapshots for both tasks. At the top, a cylindrical silicone tube of external diameter 6 mm and length 8 mm is grasped by a single arm and placed on numbered pegs. In the bottom image, the two arms are used for a stitching task. The right side grasps a circular needle and inserts it through a phantom tissue. On the left side, a Maryland end-effector is used to press the tissue against the needle. After the needle is extracted with the right hand, the needle is passed to the left hand to start the next stitching sequence. In both cases, the proposed RST could provide dexterous motion and enough grasping force to firmly grasp the objects.

V. CONCLUSION

Robotic surgical tools define the levels of dexterity of robotic systems in minimally invasive surgery. However, they still represent a high cost with few commercially available tools designed for specific hardware. Recent advances in new biocompatible materials for 3D printing open up an important opportunity for the development of innovative surgical tools. In this work, we introduced OpenRST, an open platform for customizable 3D-printed robotic surgical tools. The proposed design includes a 3-DOF en-effector design with a decoupled wrist for independent joint control, a detachable tool interface module, and a drive unit with a rapid tool exchange mechanism. A biocompatible material was chosen for manufacturing and FEA analysis was performed to verify the stress limits supported by the end-effector. Experimental validation demonstrates the ability of the proposed design to provide high grip and pulling forces. The mean absolute tracking angle error for the yaw joint is approximately 0.1 rad. We also demonstrate the usability of OpenRST in surgical training tasks such as pick-and-place and stitching. The mechanical and controller designs are open source and freely available. We hope that this work will contribute to the acceleration and expansion of the development of RMIS technologies.

APPENDICES A GENERAL SOLUTION FOR FINDING THE TANGENTIAL POINTS

Given two non-intersecting circumferences defined as

$$\zeta_1 : (\zeta_x - h_1)^2 + (\zeta_y - k_1)^2 = r_1^2 \tag{16}$$

$$\zeta_2 : (\zeta_x - h_2)^2 + (\zeta_y - k_2)^2 = r_2^2 \tag{17}$$

with $(h_{1,2}, k_{1,2})$ and $r_{1,2}$ representing the respective circumference center coordinates and radius, and a line tangent to both circumferences defined as:

$$\mathcal{L}_t : \zeta_y = \alpha \zeta_x + \beta, \tag{18}$$

we aim to find the points (b_x, b_y) and (c_x, c_y) at which $\mathcal{L}_t$ intersects ζ_1 and ζ_2, respectively.

The slope α can be found by deriving (16) and (17) as:

$$\alpha = -\frac{b_x - h_1}{b_y - k_1} = -\frac{c_x - h_2}{c_y - k_2} \tag{19}$$

Replacing Eq. (19) in Eq. (18) for b and c we get the following relation:

$$c_y + c_x \frac{c_x - h_2}{c_y - k_2} = b_y + b_x \frac{b_x - h_1}{b_y - k_1} \tag{20}$$

Using Fig. 3 for visual representation, the coordinates b can be represented as a function of the inscribed angle ϕ_1 as:

$$\begin{aligned} b_x &= h_1 + r_1 \cos\phi_1 \\ b_y &= k_1 + r_1 \sin\phi_1 \end{aligned} \tag{21}$$

The coordinates of point c are determined as $c = \zeta_{2_c} \pm r_2 \mu_\phi$, where ζ_{2_c} denotes the coordinates of the center of ζ_2, and μ_ϕ represents the unit vector from ζ_{1_c} to b. Two tangential

intersection points c can be found in ζ_2 depending on the direction of μ_ϕ

$$\begin{aligned} c_x &= h_2 + r_2 \cos\phi_1 \\ c_y &= k_2 + r_2 \sin\phi_1, \end{aligned} \tag{22}$$

and

$$\begin{aligned} c_x &= h_2 - r_2 \cos\phi_1 \\ c_y &= k_2 - r_2 \sin\phi_1. \end{aligned} \tag{23}$$

Taking the first solution for c and replacing (21) and (22) in (20), we obtain the following simplified equation.

$$(k_2 - k_1)\sin\phi_1 + (h_2 - h_1)\cos\phi_1 - r_1 - r_2 = 0 \tag{24}$$

Solving this equation, the following solution for ϕ_1 is obtained:

$$\phi_1 = \mp 2\arctan\left(\frac{\mp k_1 \pm k_2 + \sqrt{N}}{h_1 - h_2 - r_1 + r_2}\right) \tag{25}$$

where $N = (h_1 - h_2)^2 + (k_1 - k_2)^2 - (r_1 - r_2)^2$.

Following the same approach for the second solution of c,

$$\phi_1 = \pm 2\arctan\left(\frac{\mp k_1 \pm k_2 + \sqrt{M}}{h_2 - h_1 + r_1 + r_2}\right), \tag{26}$$

where $M = (h_1 - h_2)^2 + (k_1 - k_2)^2 - (r_1 + r_2)^2$.

Four solutions can be found; each solution corresponds to one of the four distinct lines that are tangent to both circumferences: two external and two internal. Fig. 3 shows the case of an internal tangent line, while Fig. 4 shows the case of an external tangent line.

REFERENCES

[1] J. Colan, A. Davila, and Y. Hasegawa, "A review on tactile displays for conventional laparoscopic surgery," *Surgeries*, vol. 3, no. 4, pp. 334–346, Nov. 2022.
[2] G. S. Guthart and J. K. Salisbury, "The Intuitive telesurgery system: Overview and application," in *Proc. IEEE Int. Conf. Robot. Automation. Symposia (ICRA)*, Apr. 2000, pp. 618–621.
[3] J. Colan, J. Nakanishi, T. Aoyama, and Y. Hasegawa, "A cooperative human–robot interface for constrained manipulation in robot-assisted endonasal surgery," *Appl. Sci.*, vol. 10, no. 14, p. 4809, Jul. 2020.
[4] C. Freschi, V. Ferrari, F. Melfi, M. Ferrari, F. Mosca, and A. Cuschieri, "Technical review of the da Vinci surgical telemanipulator," *Int. J. Med. Robot. Comput. Assist. Surg.*, vol. 9, no. 4, pp. 396–406, Dec. 2013.
[5] Y. Chen, S. Zhang, Z. Wu, B. Yang, Q. Luo, and K. Xu, "Review of surgical robotic systems for keyhole and endoscopic procedures: State of the art and perspectives," *Frontiers Med.*, vol. 14, no. 4, pp. 382–403, Aug. 2020.
[6] D. T. Wallace, C. A. Julian, T. A. Morley, and D. S. Baron, "Surgical tools for use in minimally invasive telesurgical applications," U.S. Patent 6 936 042, Aug. 30, 2005.
[7] S. Thielmann, U. Seibold, R. Haslinger, G. Passig, T. Bahls, S. Jörg, M. Nickl, A. Nothhelfer, U. Hagn, and G. Hirzinger, "MICA—A new generation of versatile instruments in robotic surgery," in *Proc. IEEE/RSJ Int. Conf. Intell. Robots Syst.*, Oct. 2010, pp. 871–878.
[8] W. Wang, J. Li, S. Wang, H. Su, and X. Jiang, "System design and animal experiment study of a novel minimally invasive surgical robot," *Int. J. Med. Robot. Comput. Assist. Surg.*, vol. 12, no. 1, pp. 73–84, Mar. 2016.
[9] B. R. Chaplin, K. Marshall, and L. D. R. Hares, "Surgical instrument articulation," U.S. Patent 10 624 703, Apr. 21, 2021.
[10] M. B. Hong and Y.-H. Jo, "Design of a novel 4-DOF wrist-type surgical instrument with enhanced rigidity and dexterity," *IEEE/ASME Trans. Mechatronics*, vol. 19, no. 2, pp. 500–511, Apr. 2014.
[11] B. Zhang, Z. Liao, P. Yang, and H. Liao, "Robotic visible forceps manipulator with a novel linkage bending mechanism," *J. Mech. Robot.*, vol. 11, no. 1, Feb. 2019.
[12] H. Wang, S. Wang, and S. Zuo, "Development of visible manipulator with multi-gear array mechanism for laparoscopic surgery," *IEEE Robot. Autom. Lett.*, vol. 5, no. 2, pp. 3090–3097, Apr. 2020.
[13] P. Francis, K. W. Eastwood, V. Bodani, K. Price, K. Upadhyaya, D. Podolsky, H. Azimian, T. Looi, and J. Drake, "Miniaturized instruments for the da Vinci research kit: Design and implementation of custom continuum tools," *IEEE Robot. Autom. Mag.*, vol. 24, no. 2, pp. 24–33, Jun. 2017.
[14] R. Robert, D. A. Zitnick, P. J. K. Cameron, L. M. Faria, and A. Bajo, "Articulated tool positioner and system employing same," U.S. Patent 11 369 353, Jun. 8, 2022.
[15] C. Girerd and T. K. Morimoto, "Design and control of a hand-held concentric tube robot for minimally invasive surgery," *IEEE Trans. Robot.*, vol. 37, no. 4, pp. 1022–1038, Aug. 2021.
[16] J. Arata, Y. Fujisawa, R. Nakadate, K. Kiguchi, K. Harada, M. Mitsuishi, and M. Hashizume, "Compliant four degree-of-freedom manipulator with locally deformable elastic elements for minimally invasive surgery," in *Proc. Int. Conf. Robot. Autom. (ICRA)*, May 2019, pp. 2663–2669.
[17] D. Haraguchi, T. Kanno, K. Tadano, and K. Kawashima, "A pneumatically driven surgical manipulator with a flexible distal joint capable of force sensing," *IEEE/ASME Trans. Mechatronics*, vol. 20, no. 6, pp. 2950–2961, Dec. 2015.
[18] Y. Yang, J. Li, K. Kong, and S. Wang, "Design of a dexterous robotic surgical instrument with a novel bending mechanism," *Int. J. Med. Robot. Comput. Assist. Surgery*, vol. 18, no. 1, p. e2334, Feb. 2022.
[19] Z. Y. Shi, D. Liu, and T. M. Wang, "A shape memory alloy-actuated surgical instrument with compact volume," *Int. J. Med. Robot. Comput. Assist. Surgery*, vol. 10, no. 4, pp. 474–481, Dec. 2014.
[20] H. M. Le, T. N. Do, and S. J. Phee, "A survey on actuators-driven surgical robots," *Sens. Actuators A, Phys.*, vol. 247, pp. 323–354, Aug. 2016.
[21] C.-H. Kuo, J. S. Dai, and P. Dasgupta, "Kinematic design considerations for minimally invasive surgical robots: An overview," *Int. J. Med. Robot. Comput. Assist. Surgery*, vol. 8, no. 2, pp. 127–145, Jun. 2012.
[22] B. Zhao and C. A. Nelson, "Decoupled cable-driven grasper design based on planetary gear theory," *J. Med. Devices*, vol. 7, no. 2, Jun. 2013.
[23] B. Zhao and C. A. Nelson, "Estimating tool–tissue forces using a 3-degree-of-freedom robotic surgical tool," *J. Mech. Robot.*, vol. 8, no. 5, pp. 0510151–05101510, Oct. 2016.
[24] K. Nishizawa and K. Kishi, "Development of interference-free wire-driven joint mechanism for surgical manipulator systems," *J. Robot. Mechatronics*, vol. 16, no. 2, pp. 116–121, 2004.
[25] D. J. Podolsky, E. Diller, D. M. Fisher, K. W. W. Riff, T. Looi, J. M. Drake, and C. R. Forrest, "Utilization of cable guide channels for compact articulation within a dexterous three Degrees-of-Freedom surgical wrist design," *J. Med. Devices*, vol. 13, no. 1, Mar. 2019.
[26] M. Jinno, "Simple noninterference mechanism between the pitch and yaw axes for a wrist mechanism to be employed in robot-assisted laparoscopic surgery," *ROBOMECH J.*, vol. 6, no. 1, pp. 1–12, Dec. 2019.
[27] K. Chandrasekaran and A. Thondiyath, "Design of a tether-driven minimally invasive robotic surgical tool with decoupled degree-of-freedom wrist," *Int. J. Med. Robot. Comput. Assist. Surgery*, vol. 16, no. 3, p. e2084, Jun. 2020.
[28] A. J. Spiers, H. J. Thompson, and A. G. Pipe, "Investigating remote sensor placement for practical haptic sensing with EndoWrist surgical tools," in *Proc. IEEE World Haptics Conf. (WHC)*, Jun. 2015, pp. 152–157.
[29] A. H. H. Hosseinabadi and S. E. Salcudean, "Force sensing in robot-assisted keyhole endoscopy: A systematic survey," *Int. J. Robot. Res.*, vol. 41, no. 2, pp. 136–162, Feb. 2022.
[30] P. S. Zarrin, A. Escoto, R. Xu, R. V. Patel, M. D. Naish, and A. L. Rejos, "Development of a 2-DOF sensorized surgical grasper for grasping and axial force measurements," *IEEE Sensors J.*, vol. 18, no. 7, pp. 2816–2826, Apr. 2018.
[31] A. L. Trejos, A. Escoto, D. Hughes, M. D. Naish, and R. V. Patel, "A sterilizable force-sensing instrument for laparoscopic surgery," in *Proc. 5th IEEE RAS/EMBS Int. Conf. Biomed. Robot. Biomechtron.*, Aug. 2014, pp. 157–162.
[32] C. Shi, M. Li, C. Lv, J. Li, and S. Wang, "A high-sensitivity fiber Bragg grating-based distal force sensor for laparoscopic surgery," *IEEE Sensors J.*, vol. 20, no. 5, pp. 2467–2475, Mar. 2020.

[33] D. C. W. Friedman, "Scaling laws and size thresholds for minimally invasive surgical instruments," Ph.D. thesis, Dept. Elect. Eng., Univ. Washington, Seattle, WA, USA, 2011.
[34] Formlabs. *Formlabs BioMed Amber Resin: Material Data Sheet*. Accessed: Aug. 15, 2022. [Online]. Available: https://formlabs-media.formlabs.com/datasheets/2001403-TDS-ENUS-0.pdf
[35] J. J. O'Neill, T. K. Stephens, and T. M. Kowalewski, "Evaluation of torque measurement surrogates as applied to grip torque and jaw angle estimation of robotic surgical tools," *IEEE Robot. Autom. Lett.*, vol. 3, no. 4, pp. 3027–3034, Oct. 2018.
[36] C. Lee, Y. H. Park, C. Yoon, S. Noh, C. Lee, Y. Kim, H. C. Kim, H. H. Kim, and S. Kim, "A grip force model for the da Vinci end-effector to predict a compensation force," *Med. Biol. Eng. Comput.*, vol. 53, no. 3, pp. 253–261, Mar. 2015.
[37] A. Abiri, J. Pensa, A. Tao, J. Ma, Y.-Y. Juo, S. J. Askari, J. Bisley, J. Rosen, E. P. Dutson, and W. S. Grundfest, "Multi-modal haptic feedback for grip force reduction in robotic surgery," *Sci. Rep.*, vol. 9, no. 1, pp. 1–10, Mar. 2019.
[38] Y. Dai, "Grasper integrated miniaturized tri-axial force sensor system for robotic minimally invasive surgery," Ph.D. thesis, Dept. Elect. Comput. Eng., Univ. California, Los Angeles, CS, USA, 2018.
[39] S. Chitta, E. Marder-Eppstein, W. Meeussen, V. Pradeep, A. R. Tsouroukdissian, J. Bohren, D. Coleman, B. Magyar, G. Raiola, M. Lüdtke, and E. F. Perdomo, "ROS_control: A generic and simple control framework for ROS," *J. Open Source Softw.*, vol. 2, no. 20, p. 456, 2017.
[40] E. Rohmer, S. P. N. Singh, and M. Freese, "V-REP: A versatile and scalable robot simulation framework," in *Proc. IEEE/RSJ Int. Conf. Intell. Robots Syst. (IROS)*, Nov. 2013, pp. 1321–1326.
[41] S. M. Khadem, S. Behzadipour, A. Mirbagheri, and F. Farahmand, "A modular force-controlled robotic instrument for minimally invasive surgery–efficacy for being used in autonomous grasping against a variable pull force," *Int. J. Med. Robot. Comput. Assist. Surgery*, vol. 12, no. 4, pp. 620–633, Dec. 2016.
[42] J. Colan, J. Nakanishi, T. Aoyama, and Y. Hasegawa, "Optimization-based constrained trajectory generation for robot-assisted stitching in endonasal surgery," *Robotics*, vol. 10, no. 1, p. 27, Feb. 2021.

JACINTO COLAN (Member, IEEE) received the B.S. degree from the National University of Engineering, Lima, Peru, in 2010, and the M.E. and Ph.D. degrees in micro-nano mechanical science and engineering from Nagoya University, Nagoya, Japan, in 2018 and 2021, respectively. He is currently a Postdoctoral Researcher with Nagoya University. His main research interests include medical robotics, human–robot interfaces, and intelligent assistive systems. He received the Best Paper Award from the IEEE International Symposium on Micro-NanoMechatronics and Human Science (MHS 2019 and MHS 2022).

ANA DAVILA (Member, IEEE) received the B.E. degree from the National University of San Antonio Abad of Cusco, Cusco, Peru, in 2009, the M.S. degree in life science from Kyoto University, Japan, in 2018, and the Ph.D. degree in medical sciences from Osaka University, Japan, in 2022. She is currently a Postdoctoral Researcher with Nagoya University, Japan. Her main research interests include intelligent systems, human–robot interaction, medical robotics, and bioinformatics.

YAONAN ZHU (Member, IEEE) received the B.S. degree from Northeastern University, China, in 2015, the M.S. degree from the University of Science and Technology of China, in 2018, and the Ph.D. degree in robotics from Nagoya University, Japan, in 2021. He is currently a Designated Assistant Professor with Nagoya University. His main research interests include telerobotics and teleoperation, haptics and haptic interfaces, human-centered robotics, and wearable robotics.

TADAYOSHI AOYAMA (Member, IEEE) received the B.E. degree in mechanical engineering, the M.E. degree in mechanical science engineering, and the Ph.D. degree in micro-nano systems engineering from Nagoya University, Nagoya, Japan, in 2007, 2009, and 2012, respectively. He was an Assistant Professor at Hiroshima University, Japan, from 2012 to 2017, and Nagoya University, Japan, from 2017 to 2019. He was also a PRESTO Researcher at JST, from 2018 to 2022. He is currently an Associate Professor with the Department of Micro-Nano Mechanical Science and Engineering, Nagoya University. His research interests include macro-micro interaction, VR/AR and human interface, AI-based assistive technology, micro-manipulation, and medical robotics.

He received the Best Paper Award from the 2019 IEEE/ASME International Conference on Advanced Intelligent Mechatronics (AIM2019) and the IEEE International Symposium on Micro-NanoMechatronics and Human Science (MHS2017, MHS2019, and MHS2022).

YASUHISA HASEGAWA (Member, IEEE) received the B.E., M.E., and Ph.D. degrees in robotics from Nagoya University, Nagoya, Japan, in 1994, 1996, and 2001, respectively. From 1996 to 1998, he was at Mitsubishi Heavy Industries Ltd., Japan. He joined Nagoya University, in 1998. He moved to Gifu University, in 2003. From 2004 to 2014, he was with the University of Tsukuba. Since 2014, he has been with Nagoya University, where he is currently a Professor with the Department of Micro-Nano Systems Engineering. His main research interests include motion-assistive systems, teleoperation for manipulation, and surgical support robot.